01 Jan 2023

Intragranular Nanocomposite Powders As Building Blocks For Ceramic Nanocomposites

Ryan D. Dempsey

Xiaoqing He

Jonathan A. Scott

David W. Lipke
Missouri University of Science and Technology, lipked@mst.edu

Recommended Citation

R. D. Dempsey et al., "Intragranular Nanocomposite Powders As Building Blocks For Ceramic Nanocomposites," *Journal of the American Ceramic Society*, Wiley, Jan 2023.
The definitive version is available at https://doi.org/10.1111/jace.19175

Received: 11 August 2022 | Revised: 5 March 2023 | Accepted: 16 April 2023

DOI: 10.1111/jace.19175

Journal of the American Ceramic Society

RESEARCH ARTICLE

Intragranular nanocomposite powders as building blocks for ceramic nanocomposites

Ryan D. Dempsey[1] | **Xiaoqing He**[2] | **Jonathan A. Scott**[1,#] | **David W. Lipke**[1,#]

[1]Department of Materials Science & Engineering, Missouri University of Science and Technology, Rolla, Missouri, USA

[2]Electron Microscopy Core and Department of Mechanical & Aerospace Engineering, University of Missouri, Columbia, Missouri, USA

Correspondence
David W. Lipke, Department of Materials Science & Engineering, Missouri University of Science and Technology, Rolla, MO 65409, USA.
Email: Lipke@mst.edu

[#]Member, American Ceramic Society.

Funding information
U. S. Army Research Laboratory and the U. S. Army Research Office, Grant/Award Number: W911NF-14-1-0560

Editor's Choice
The Editor-in-Chief recommends this outstanding article.

Abstract

A powder-based bottom-up processing scheme is introduced for the production of ceramic nanocomposites. Internal displacement reactions between solid solution powders and metallic reactants proceeding via gaseous intermediates are utilized to generate nanostructured building blocks for the synthesis of ceramic nanocomposites. Subsequent rapid sintering results in ceramic nanocomposites, whose microstructures are inherited from the building blocks. This processing scheme is demonstrated for the production of titanium carbide nanocomposites featuring up to 28 wt.% intragranular tungsten inclusions derived from titanium-tungsten mixed carbide powders. Heat treatment of mixed carbide powders in evacuated ampoules containing titanium sponge and iodine at 1000°C for 24 h resulted in nanocomposite powders featuring tungsten precipitates within titanium carbide grains that were subsequently consolidated via spark plasma sintering at 1300°C for 10 min to produce titanium carbide/metallic tungsten nanocomposites. Transformation of mixed titanium–tungsten carbide powders to titanium carbide/metallic tungsten nanocomposite powders was analyzed via X-ray diffraction. Electron microscopy observations of microstructures pre- and post- sintering showed that the intragranular character of nanocomposite powders can be retained in sintered ceramic nanocomposites. The building block approach demonstrated in this work represents an improved method to make ceramic nanocomposites with majority intragranular character.

KEYWORDS
carbides, nanocomposites, precipitates/precipitation, processing, synthesis

1 | INTRODUCTION

Ceramic "nanocomposites" have been a recurring subject of interest owing to reported increases in apparent strength[1–5] upon incorporation of nanodispersed second-phase reinforcements. Crack front interactions with misfitting inclusions and their associated bulk[6,7] and surface[8,9] residual stresses are thought to be responsible for modifying the fracture behavior of these materials. Fracture mechanic approaches have been employed to better understand structure–property tradeoffs and to establish guiding principles for microstructure design of ceramic "nanocomposites".[10–12] Critical reviews have examined how reinforcement type, size, amount, and location relative to grain boundaries (i.e., inter- vs. intra-granular) can significantly affect material behavior, illustrative of the complex relationships between microstructure, residual stresses, and fracture in brittle heterogeneous materials.[13–21] Some researchers argue that it is in this complex landscape, yet to be fully explored or understood, that

there exists opportunity for development of ceramics and ceramic composites that are exceptionally strong, tough, and reliable.[22–26]

Microstructure design of heterogeneous "nanocomposites" is also of interest for electronic and other functional ceramics. For example, nanometric inclusions can enhance ferroelectric performance via domain size refinement,[27,28] while the incorporation of metallic inclusions in an electrically insulating matrix can increase dielectric permittivity by orders of magnitude via interfacial polarization effects.[29,30] Piezoelectric nanocomposites have also been designed to more effectively couple electrical–mechanical responses by preferentially locating metallic nanoinclusions within piezo-active grains.[31]

Researchers studying ceramic "nanocomposites" have developed methods to control microstructures for material systems of interest, including Al_2O_3–SiC,[2,32] Si_3N_4–SiC,[1,33] and various metal–metal oxide composites.[3,20,34–42] These methods generally fall into one of the two categories: particle occlusion via grain growth, or displacement reaction-induced phase transformations. The first method (particle occlusion) exploits grain boundaries whose velocity is sufficiently fast to detach from fine second-phase particles as they sweep through a material region. Such high velocities have been achieved by enhancing mobility in the presence of a glass or liquid grain boundary phase[39] or by providing large thermodynamic driving forces such as that found during matrix recrystallization.[32]

The second method (phase transformation) employs gas–, liquid–, or solid–solid displacement reactions to introduce heterogeneities via solid-state precipitation. Solid–solid reactions (e.g., reaction sintering) are commonly employed to produce multiphase ceramics and ceramic composites.[43–45] Solid–solid reactions initiate at particle–particle contacts; therefore, the homogeneity of mixing of reactants at the granular scale is critical to attaining complete and uniform reaction, often requiring sintering temperatures in excess of 1500°C.[15] A major disadvantage of solid–solid reactions for the production of ceramic nanocomposites is that the homogeneity of mixing becomes increasingly difficult to maintain at the nanoscale due to agglomeration. Reported attempts to produce ceramic nanocomposites via reaction sintering-based approaches illustrate the challenges in attaining granular-scale homogeneity of nanostructures.[46–48]

Solid–solid reactions can be mediated via fluid phases (i.e., gas or liquid) to more effectively transport reactants to solid interfaces. This is most commonly practiced via reactive melt infiltration; however, melt infiltration has the drawback of residual solidified melt dispersed throughout the resulting composite.[49] While recent research suggests that spontaneous formation of a wetting liquid at interparticle contacts can greatly enhance the rate of solid-state reactions,[50] the general applicability of this approach to nanocomposite synthesis has not been explored. Alternatively, solid–solid displacement reactions can be promoted via gaseous phase intermediates.[37,51,52] The gas-phase mediated approach to nanocomposite synthesis possesses several notable advantages over liquid– and solid–solid reaction routes, including the avoidance of deleterious solidified byproducts and of interparticle contact issues, respectively.

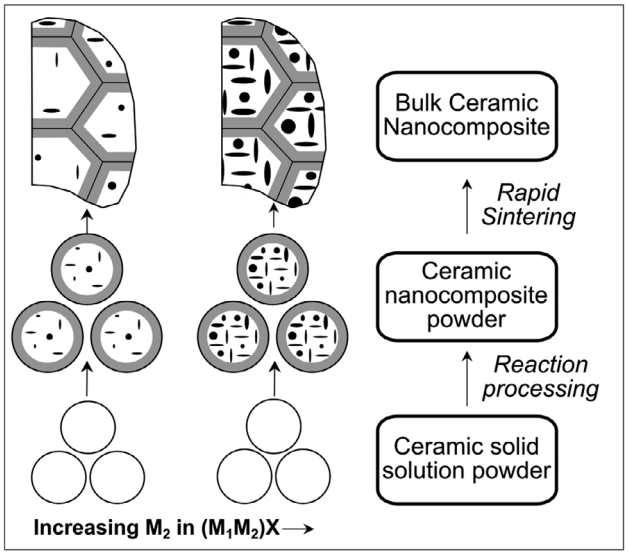

FIGURE 1 Schematic illustration of key processing steps to fabricate ceramic nanocomposites with majority intragranular character.

Figure 1 schematically illustrates a powder-based bottom-up fabrication scheme to produce ceramic nanocomposites. Beginning with ceramic solid solution powders, selective displacement reactions induce the formation of nanodispersed precipitates within the matrix of each primary particle grain. Specifically, the fabrication scheme employed in this work to generate nanostructured powders utilizes metallothermic displacement reactions of the type $M_1 + (M_1M_2)X \rightarrow M_1X + M_2$, where reactant M_1 is transported via gaseous halide intermediates to the solid interface on $(M_1M_2)X$ particles, where X = B, C, N, or O. These intragranular nanocomposite powders are subsequently used as feedstock for conventional powder processing to produce ceramic nanocomposites. The use of metallothermic displacement reactions to synthesize nanocomposite powders and the subsequent retention of nanostructures via rapid sintering technique are key innovations to produce ceramic nanocomposites with majority intragranular character.

To demonstrate the proposed scheme, this report describes the fabrication of intragranular titanium carbide nanocomposites featuring up to 28 wt.% tungsten reinforcements. In the first processing step,

commercially available $(Ti_{1-x}W_x)C$ solid solution powders are heat treated in liquid aluminum to enhance their crystallinity and chemical homogeneity.[53] Then, using a halide-mediated metallothermic displacement reaction, $(Ti_{1-x}W_x)C$ powders with WC content (x) ranging from 0.00 to 0.21 were reactively converted to nanocomposite powders. The overall reaction can be represented as shown in Equation (1):

$$(Ti_{1-x}W_x)C_y + \left[(x-x') + (y-y')/y'\right]\ \{Ti\}(g)$$
$$\underbrace{(Ti_{1-x'}W_{x'})C_{y'} + (x-x')\ W}_{\text{core}} + \underbrace{\left[(y-y')/y'\right]\ TiC_{y'}}_{\text{cladding}} \quad (1)$$

where {Ti}(g) denotes titanium transported through the gas phase as any titanium iodide intermediate species (i.e., TiI_z where z = 1–4), and where x, y and x', y' are the initial and final fractions of tungsten and carbon on their lattice sites, respectively. The underscoring notations in Equation (1) refer to microstructural locations in the product intragranular nanocomposite powders composed of two regions: a core consisting of metallic tungsten precipitates in a tungsten-depleted TiC-based matrix and an epitaxially deposited TiC cladding layer devoid of precipitates. A more detailed description of the thermodynamics and morphological development of intragranular nanocomposite powders has been previously reported.[51] These intragranular nanocomposite powders were subsequently chemically treated to remove any non-intragranular metal and consolidated via spark plasma sintering to produce ceramic nanocomposites. This work presents materials characterization results that illustrate the evolution of microstructure at each processing step to establish processing–microstructure relationships in the production of ceramic nanocomposites from intragranular nanocomposite powder building blocks.

2 | MATERIALS AND METHODS

2.1 | Preparation of intragranular nanocomposite powders

$(Ti_{1-x}W_x)C$ solid solution powder compositions of x = 0.00, 0.06, 0.11, 0.15, and 0.21 were prepared via aluminum metal flux crystallization in accordance with previously published procedures[53] and subsequently blended with titanium sponge (Atlantic Equipment Engineers, 99.7%, −16+30 mesh) in a mass ratio of 1.36:1 and placed in a one-end closed fused silica tube (~200 mm length × 10.50 mm inner diameter × 12.75 mm outer diameter). Iodine crystals (Acros Organics, resublimed, 99.5% purity) were added in a mass ratio of 1:3.66 relative to the titanium sponge, and the tube was subsequently evacuated to ~5 mbar pressure for 1 h and then sealed via heating with an oxypropane torch. The sealed ampoule was then heat treated at 1000°C for up to 24 h.

Product materials were recovered by scoring and breaking the heat-treated ampoules. Recovered products were subjected to multiple rinses in ethanol, 10 wt.% solution of sodium metabisulfite in water (Fisher Scientific, 99.4%), and water. Unreacted titanium sponge and debris from the broken ampoule were separated from the powders using No. 325 and 600 sieves. The fraction of intragranular metal in the W–$TiC_{y'}$ powders was assessed by treating powder in 6N sodium hydroxide solution at 80–100°C for ~3 h and characterizing the phase composition of the resulting powder by X-ray diffraction (XRD) analysis.

2.2 | Rapid sintering of ceramic nanocomposites

Nanocomposite powders were consolidated via spark plasma sintering (Model HP D25, FCT Systeme GmbH) in 1 cm graphite dies lined with boron nitride-coated graphite foil. Samples were subjected to the following heat treatment schedule performed under vacuum: heating at 100°C/min to 800°C, dwelling for 5 min, continuing to heat at 100°C/min to 1300°C, dwelling for 10 min, and cooling to 800°C at 100°C/min at which point the furnace power was terminated. An initially applied pressure of 6.25 MPa was increased incrementally up to 40 MPa and maintained for temperatures above 800°C. After recovery of the consolidated pellets from the graphite die, ~0.2–0.5 mm of material was ground from each face of the sample to remove flashing.

2.3 | Materials characterization

Ceramic nanocomposites were prepared for microstructural analysis by grinding and polishing to a 0.25 μm diamond finish followed by vibratory polishing for ~24 h. Sample densities were measured via the Archimedes method using water as an immersion medium. Phase compositions of product materials were determined by XRD on a Bragg–Brentano style diffractometer (Philips MPD-XPERT, Malvern Panalytical, Westborough, MA) using Cu-Kα radiation over a measurement range of 10°–138° 2θ with a step size of 0.026° 2θ. Quantitative phase analysis was performed using a commercial Rietveld refinement analysis package (RIQAS 4, Materials Data, Inc., Livermore, CA) taking as inputs the expected equilibrium compositions computed with a commercial

thermodynamics software package (FactPS and SpMCBN databases, FactSage, Montreal, Canada).[54] Carbon stoichiometry (y) values for mixed carbide solution phases were established using the tungsten (1 0 0) peak to correct for specimen displacement. These stoichiometry values were used in combination with XRD peak area values to calculate theoretical densities for each ceramic nanocomposite specimen.

Microstructural analysis of nanocomposite powders was performed on a dual focused ion beam (FIB) scanning electron microscope (SEM) (FEI Scios, Hillsboro, OR, USA). SEM images were taken at 5 kV in secondary electron collection mode using 100 pA current. FIB milling/polishing was employed to section individual particles and revealed their internal features. FIB milling was also employed to produce an electron-transparent slice for transmission electron microscopy (TEM) analysis (FEI Tecnai F30 Twin 300 kV TEM equipped with a Bruker 30 mm^2 active area Silicon Drift Detector with superlight element window for energy dispersive spectroscopy (EDS), Hillsboro, OR, USA) using previously published procedures.[55] Scanning transmission electron microscopy (STEM) images were collected in high angle annular dark field (HAADF) mode to highlight precipitate distributions. The relative phase intensities observed in STEM–HAADF images are proportional to average phase atomic number $|Z|^{1.7}$.[56] Microstructural analysis of sintered ceramic nanocomposites was performed on a dual beam FIB/SEM (FEI Helios Nanolab 600, Hillsboro, OR, USA). Precipitate sizes (i.e., minimum and maximum Feret diameters) were measured by performing manual tracing of features revealed on cross-sectional SEM micrographs using FIJI ImageJ software.[57]

3 | RESULTS AND DISCUSSIONS

3.1 | Nanocomposite powders

Nanocomposite powders produced by displacement reactions between solid solution powders and titanium transported via gaseous halide intermediates were conducted at 1000°C for all trials. The effects of heat treatment time and starting composition of the solid solution powders on the extent of reaction were evaluated via XRD. In all cases, the product XRD patterns indicated the presence of two major phases: $(Ti_{1-x'}W_{x'})C_{y'}$ and tungsten. The results of quantitative XRD analyses (Table 1, see Figures S1–S3 for additional details) for this time series indicates that the extent of reaction as measured by the weight percentage of tungsten product increases from 3–12 h reaction times (from 9.1 to 21.8 wt.%) with complete reaction likely occurring between 12–24 h resulting in a final tungsten content of 22.5 wt.%. Consequently, for all starting materials of varying composition, fixed reaction times of 24 h were employed. On the basis of the measured weight percentages of tungsten found in the product materials, it is concluded that near-complete extent of reaction was attained for all trials.

To assess the amount of intragranular tungsten in each product material, a chemical treatment was used to digest solution-accessible metal by use of hot aqueous NaOH solutions. Intragranular tungsten is presumed to be inaccessible to the digesting solution due to encapsulation in matrix grains; therefore, the amounts of intragranular and non-intragranular tungsten could be quantified on the basis of the measured changes in weight percentages of tungsten in pre- and post-chemically treated powders. The resulting percentages of tungsten not accessible to the digesting solution are assessed to be 88%, 97%, 82%, and 91% for $x = 0.06$, 0.11, 0.15, 0.21, respectively, indicating that the majority of tungsten precipitates are indeed intragranular. This majority intragranular character is thought to be attributable to the formation of a cladding layer around each nanocomposite powder grain, a unique feature of the employed reaction shown in Equation (1). The interested reader is directed to prior work describing the origins of this morphology associated with metallothermic displacement reactions.[49,51]

FIB milling was employed to cross-section intragranular nanocomposite powder grains to reveal their internal structures. Figure 2 depicts an STEM–HAADF micrograph of a nanocomposite powder grain with initial composition of $(Ti_{0.85}W_{0.15})C$ heat treated at 1000°C for 6 h (i.e., a time insufficient to attain complete batch reaction). Intragranular phase contents were assigned on the basis of XRD analyses (Figures S1 and S2) and TEM–EDS elemental composition maps (Figure S4). The center of the particle appears bright due to increased Z-contrast indicative of increased tungsten content and contains several crystallographic defects along which preferential precipitation is observed in advance of the reaction front, but otherwise contains no visible features away from these defects. Outside the bright central region are two precipitate-containing rings: an outer ring featuring a hexagonal perimeter and an inner ring that appears ellipsoidal in the examined cross-section, that is, conformal to the bright central region. The precipitates display circular platelet-like morphologies of varying coarseness with the smallest discernable precipitates occurring in the proximity of the reaction front near the inner ring. Encapsulating the precipitate-containing regions is a conformal $TiC_{y'}$ cladding. The estimated cladding volume percentage, calculated assuming that Figure 2 illustrates a diametric cross-section, is ~40%–46% depending on whether the sectioned grain is approximated by a regular dodecahedron

TABLE 1 Summary of theoretical and measured tungsten contents and measured feature dimensions for the synthesized nanocomposite powders

Starting $(Ti_{1-x}W_x)C$ composition	wt.% W (Theoretical)	wt.% W (XRD)	wt.% W (chemically treated, XRD)	wt.% W (SEM)	Median W precipitate max. Feret diameter (nm)	Median W precipitate min. Feret diameter (nm)
$(Ti_{0.94}W_{0.06})C$	9.9	9.8	8.7	20.7	58	20
$(Ti_{0.89}W_{0.11})C$	16.7	16.4	16.0	37.5	75	24
$(Ti_{0.85}W_{0.15})C$	21.3	22.5	19.3	50.9	106	34
$(Ti_{0.79}W_{0.21})C$	28.4	27.9	26.0	44.8	95	33

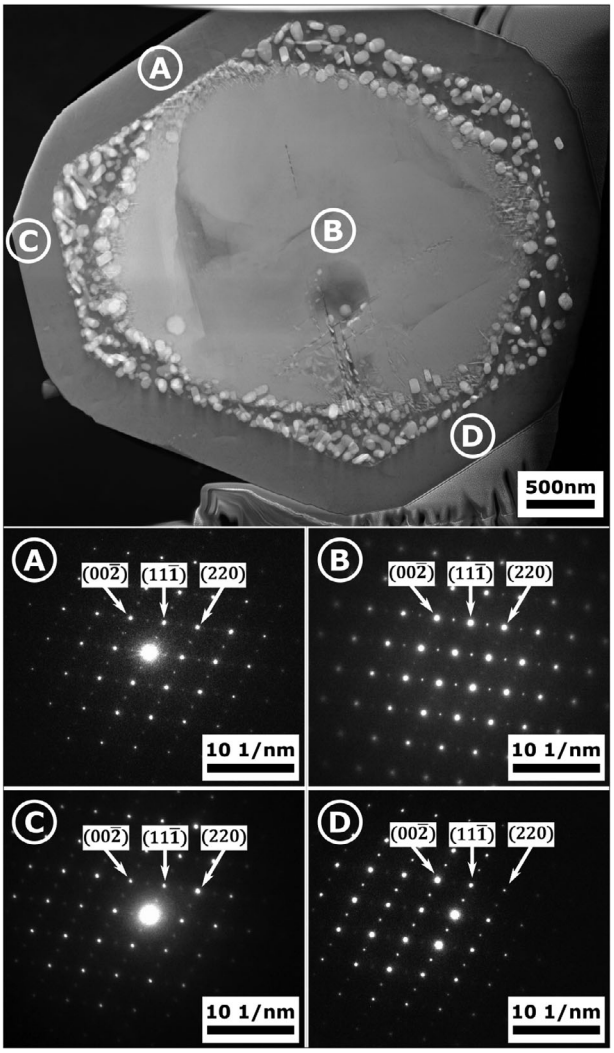

FIGURE 2 Top: STEM–HAADF micrograph of $(Ti_{0.85}W_{0.15})C$ grain reacted at 1000°C for 6 h; bottom: electron diffraction patterns collected from denoted regions of the particle, all determined to be parallel to the $(1\bar{1}0)$ zone axis of TiC. STEM–HAADF, scanning transmission electron microscopy–high angle annular dark field.

or an equivalent sphere. This estimated cladding volume percentage is close to the expected value of ~47 vol.% calculated from Equation (1) assuming $x = 0.15$ for the observed particle. Note that the volume percentage of $TiC_{y'}$ cladding as determined from Equation (1) depends solely on the extent of carbon depletion from the initial solid solution. That the observed cladding volume percentage approaches the maximum expected value likely indicates that the remaining solid solution $(Ti_{1-x'}W_{x'})C_{y'}$ in the bright central region has attained a near-minimum equilibrium value y' for carbon stoichiometry. This suggests that the examined particle may be fully reacted relative to Equation (1), but that the morphological evolution was captured at an intermediate stage. The precipitate-containing rings represent the final nanocomposite powder microstructure, whereas the bright central region comprises either a supersaturated solid solution whose tungsten content x' exceeds the equilibrium value or a two-phase region containing unresolved tungsten embryos. The nature of the reaction front at the boundary between the bright central region and the precipitate-containing rings remains poorly understood. If the bright central region comprises a supersaturated solid solution, then barriers to nucleation and growth may be responsible for delaying the onset of tungsten precipitate formation. On the other hand, if the bright central region contains unresolved tungsten embryos, then the reaction front could represent a discontinuous coarsening process as seen in other metal–ceramic nanocomposite systems.[36,58,59]

The crystallography of the reacted particle shown in Figure 2 was investigated by electron diffraction. Collected diffraction patterns from four regions labeled A, B, C, and D, are shown in the bottom panels of Figure 2. All collected diffraction patterns showed the presence of a single diffracting phase with $Fm\bar{3}m$ symmetry corresponding to $(Ti_{1-x'}W_{x'})C_{y'}$ in the bright central region or $TiC_{y'}$ in the cladding. The same crystallographic orientation was observed in all four locations with the main diffraction spots indexed to a [1 1 0] zone axis of TiC and faint superlattice diffractions that can be attributed to carbon sublattice effects. The consistency between patterns with minimal misorientation collected on both sides of the reaction front indicates that the particle is monocrystalline, demonstrating that the $TiC_{y'}$ cladding forms by an epitaxial mechanism. Lattice parameter values calculated from the

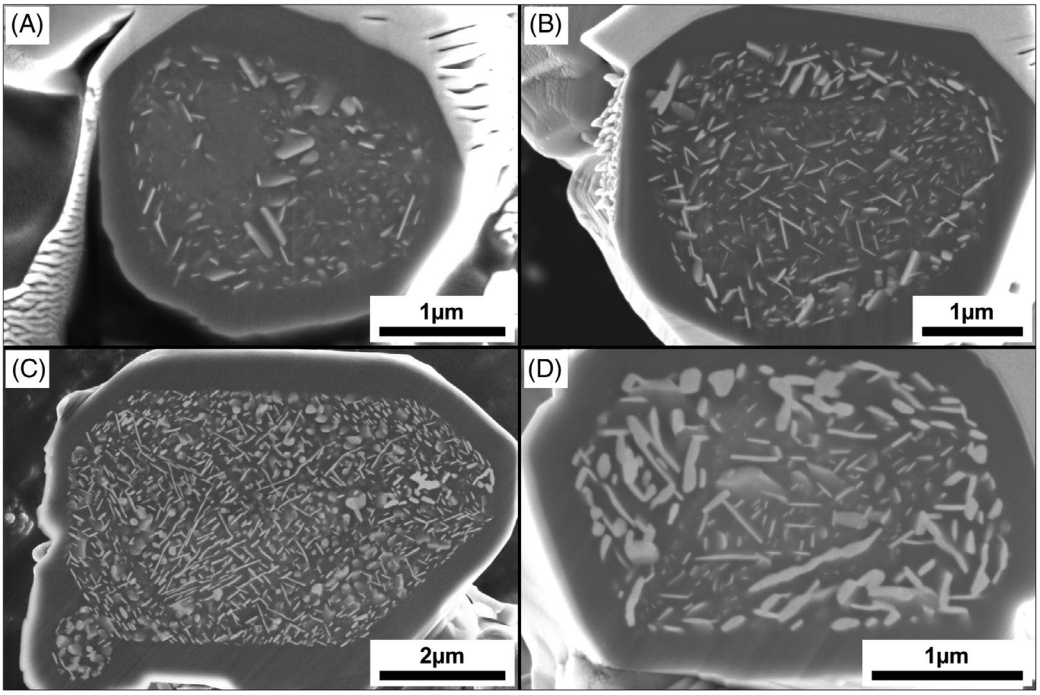

FIGURE 3 SEM micrographs of W-$TiC_{y'}$ nanocomposite powder grains, post-heat treatment in the presence of titanium iodide vapors at 1000°C for 24 h, corresponding to the following initial compositions: (a) $(Ti_{0.94}W_{0.06})C$; (b) $(Ti_{0.89}W_{0.11})C$; (c) $(Ti_{0.85}W_{0.15})C$; and, (d) $(Ti_{0.79}W_{0.21})C$. The bright phase located in particle interiors is metallic tungsten precipitates, interspersed within a darker $TiC_{y'}$ matrix. Deposited platinum from the FIB lift-out process is visible on the outermost portions of cross-sectioned particles.

diffraction patterns were consistently larger than expected, varying from 4.355–4.401Å (in contrast with 4.306 and 4.325Å for $TiC_{0.55}$ and $(Ti_{0.85}W_{0.15})C$, respectively),[60] indicating that significant lattice strain may be present.

Precipitate morphology was evaluated using TEM and FIB/SEM techniques. Cross-sectional SEM micrographs of nanocomposite powder grains with initial $(Ti_{1-x}W_x)C_y$ compositions of $x = 0.06$, 0.11, 0.15, and 0.21 after heat treatments at 1000°C for 24 h are shown in Figure 3. The nanocomposite powder grains exhibit microstructures featuring a core comprising a $(Ti_{1-x'}W_{x'})C_{y'}$ matrix with $x' \cong 0$ and y' near the sub-stoichiometric limit for the solid solution that contains tungsten platelet-like precipitates, all of which is surrounded by a conformal $TiC_{y'}$ cladding. Nanocomposite powder grains with initial $(Ti_{1-x}W_x)C_y$ compositions of $x = 0.11$, 0.15, and 0.21 and $y \cong 1$ exhibited similar precipitate distributions within any given examined powder grain, and the observed area fraction of precipitates increases with initial x values. However, for the initial $(Ti_{1-x}W_x)C_y$ composition of $x = 0.06$ and $y \cong 1$, sampling of multiple grains by FIB sectioning revealed wide variability in microstructure in terms of both precipitate location and distribution. This observation is in agreement with the reported evaluation of compositional homogeneity of the $(Ti_{1-x}W_x)C$ precursor powder by XRD line broadening analysis, which established that the $(Ti_{0.94}W_{0.06})C$ composition exhibited a range of possible WC contents spanning −83% to +100% of the average WC content after aluminum metal flux heat treatment.[53] Image analyses of FIB cross-sections of nanocomposite powders shown in Figure 3 resulted in measured area percentages of tungsten precipitates that were used to calculate equivalent weight percentages for comparison with XRD analyses. The results of this calculation are shown in Table 1, where it can be seen that the apparent tungsten percentages significantly exceed the batch values as determined by XRD analyses. The stereological approach used to calculate these equivalent weight percentages assumes that the measured area percentages of tungsten precipitates are equivalent to their volume percentages, which requires that the precipitates are randomly sampled or that they are randomly oriented in the viewing plane. In the present case, this requirement may not be satisfied due to preferred crystallographic orientations of these anisometric precipitates, resulting in overestimation of the amount of tungsten by use of cross-sectional image analyses of a limited number of FIB cross-sections.

3.2 | Ceramic nanocomposites

The results of materials characterization via XRD, Archimedes density measurements, and SEM image

TABLE 2 Measured composition parameters, density values, and precipitate feature sizes for the fabricated bulk ceramic nanocomposites

Starting $(Ti_{1-x}W_x)C$ composition	Carbon stoichiometry (y') in $(Ti_{1-x'}W_{x'})C_{y'}$	Theoretical density* ($g \cdot cm^{-3}$)	Measured density ($g \cdot cm^{-3}$)	wt.% W (XRD)	wt.% W (SEM)*	Median W precipitate max. Feret diameter (nm)	Median W precipitate min. Feret diameter (nm)
$(Ti_{1.00}W_{0.00})C$	0.62	4.61	4.46	–	–	–	–
$(Ti_{0.94}W_{0.06})C$	0.56	4.98	5.04	10.7	–	–	–
$(Ti_{0.89}W_{0.11})C$	0.51	5.18	5.28	16.1	28.7	88	44
$(Ti_{0.85}W_{0.15})C$	0.57	5.58	5.64	23.3	32.5	142	58
$(Ti_{0.79}W_{0.21})C$	0.61	5.87	5.77	28.3	44.8	121	73

*Calculated assuming phase composition comprises $(Ti_{1-x'}W_{x'})C_{y'}$ ($x' \cong 0$), ~4.61 $g \cdot cm^{-3}$ independent of carbon stoichiometry) and tungsten (19.25 $g \cdot cm^{-3}$).

analyses for ceramic nanocomposites consolidated via spark plasma sintering of nanocomposite powder grains with initial $(Ti_{1-x}W_x)C_y$ compositions of $x = 0.06$, 0.11, 0.15, and 0.21 and $y \cong 1$, as well as for a control specimen of TiC, are summarized in Table 2. The effects of consolidation heat treatment at 1300°C for 10 min on phase composition were evaluated via XRD (Figure S5). Quantitative XRD analyses indicate no significant changes in phase composition when comparing nanocomposite powders to consolidated ceramic nanocomposites.

As shown in Table 2, carbon stoichiometries (y') in $(Ti_{1-x'}W_{x'})C_{y'}$ ceramic nanocomposites were assessed by quantitative XRD analyses and confirmed to be close to the theoretical minimum equilibrium value of ~0.55 independent of the starting amount of tungsten in the solid solution. Bulk density values obtained by Archimedes method are within ± 4% of values calculated from XRD-determined phase compositions.

Cross-sectional SEM micrographs of ceramic nanocomposites consolidated by spark plasma sintering are shown in Figure 4. All specimens exhibited several percent isolated porosity which was comparable to that observed in the single-phased control specimen (Figure S6). For ceramic nanocomposites consolidated from nanocomposite powder grains with initial $(Ti_{1-x}W_x)C_y$ compositions of $x = 0.11$, 0.15, and 0.21 and $y \cong 1$, it is evident that the intragranular structure observed in the powder has been retained in the bulk. The building block nature of the ceramic nanocomposites can also be seen in Figures 4 and 5, where the majority of nanocomposite cores remain distinct and separated by what is presumed to be their former claddings. The cladding volume fraction (e.g., 47% based on Equation (1) for $x = 0.15$) in nanocomposite powder building blocks results in sintered ceramic nanocomposites featuring nanocomposite cores dispersed in a $TiC_{y'}$ matrix. The matrix volume fraction is thus inherited from the cladding volume fraction and could, in principle, be varied by judicious selection of reactant composition. For ceramic nanocomposites consolidated from nanocomposite powder grains with initial $(Ti_{1-x}W_x)C_y$ compositions of $x = 0.06$ and $y \cong 1$, the variety of structures observed in the nanocomposite powder are also preserved and produce a similar degree of morphological variation in the consolidated material.

To further characterize these ceramic nanocomposites, SEM image analyses were conducted to evaluate amounts and size distributions of tungsten inclusions. Due to the irregularity of the morphologies present in the sample having initial composition $(Ti_{0.94}W_{0.06})C$, only the samples having initial compositions $(Ti_{1-x}W_x)C_y$ with $x = 0.11$, 0.15, and 0.21 were subjected to image analysis. Table 2 indicates the resultant weight percentages of tungsten computed from apparent area percentages observed in the polished cross-sections. As was found in the case of nanocomposite powders, the resultant estimates for tungsten weight percentages significantly exceed those values estimated by XRD. Due to the similarity in microstructures between the nanocomposite powders and sintered ceramic nanocomposites, the present authors believe this to be a stereological effect of preferred orientations of anisometric precipitates.

Precipitate morphology was evaluated by manually tracing precipitates and generating distributions of minimum and maximum Feret diameters (Figure S7). All distributions are apparently log-normal and discernable coarsening can be seen when comparing these distributions across all studied compositions pre- versus post-consolidation. The extent of coarsening was quantified by evaluation of changes in the median precipitate minimum and maximum Feret diameters shown in the final columns of Tables 1 and 2. An increase of ~26% in the median maximum Feret diameter and an increase of ~92% in minimum Feret diameter are observed upon consolidation. However, the resultant sintered ceramic nanocomposites retain the majority intragranular character of the nanocomposite powders as well as the nanometric dimensions of their internal precipitate morphologies.

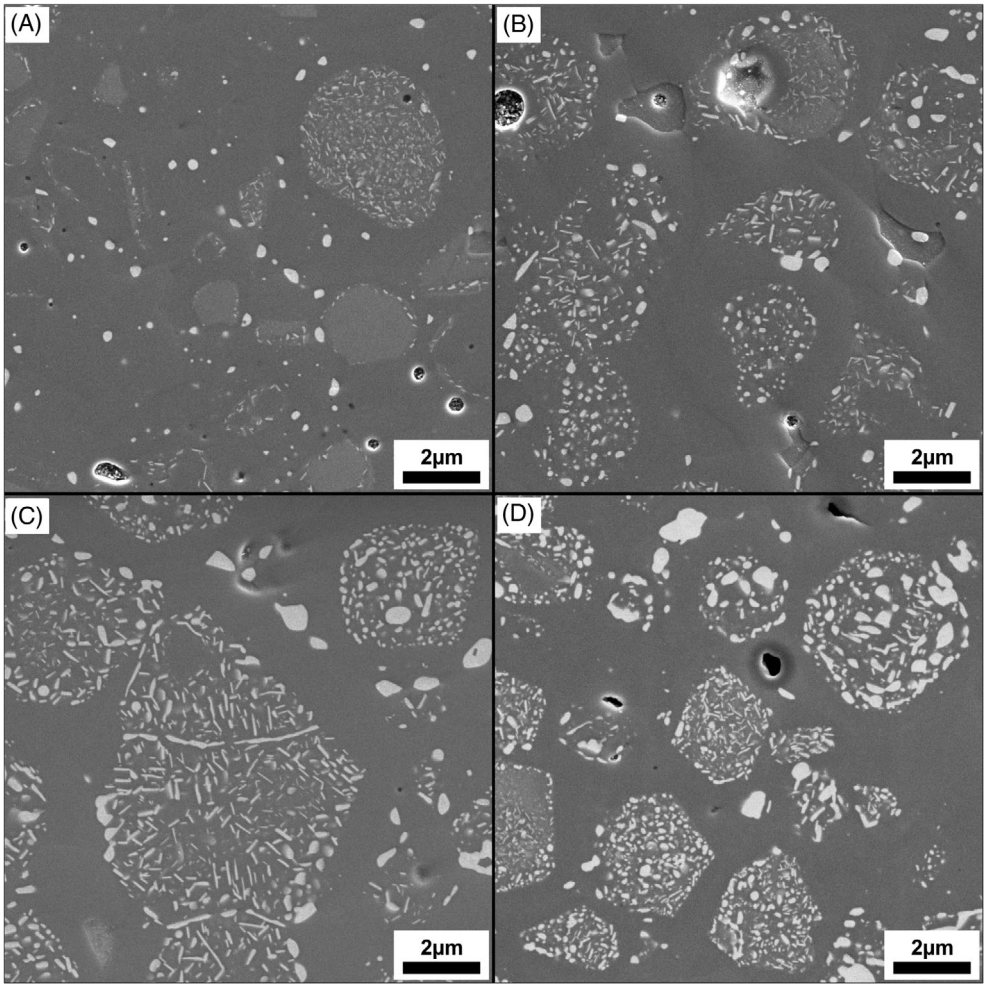

FIGURE 4 SEM micrographs of W–TiC_y ceramic nanocomposites consolidated via spark plasma sintering at 1300°C for 10 min. Panels correspond to initial compositions given by: (a) $(Ti_{0.94}W_{0.06})C$; (b) $(Ti_{0.89}W_{0.11})C$; (c) $(Ti_{0.85}W_{0.15})C$; and, (d) $(Ti_{0.79}W_{0.21})C$. Bright features correspond to metallic tungsten interspersed in a darker TiC_y matrix.

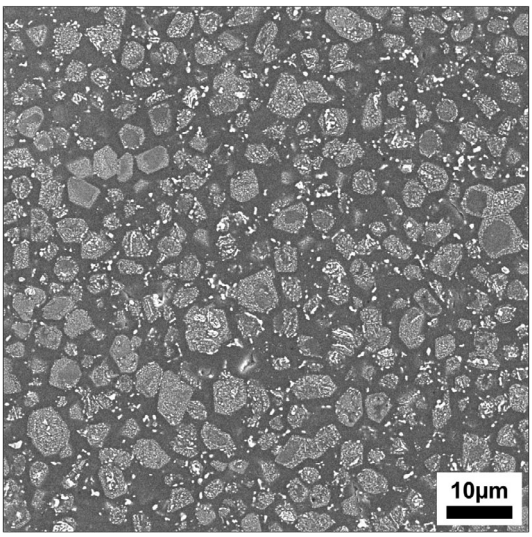

FIGURE 5 SEM micrograph of W–TiC_y ceramic nanocomposite consolidated via spark plasma sintering of reacted $(Ti_{0.85}W_{0.15})C$ nanocomposite grains.

4 | CONCLUSIONS

The building block strategy to fabricate ceramic nanocomposites via sintering of nanocomposite powders has been demonstrated. With appropriate process chemistry, the proposed strategy has broad applicability to both oxide and non-oxide ceramics, and therefore may find utility in a variety of structural and/or functional material applications. Metallothermic displacement reactions have been shown to be effective in generating nanocomposite powders with majority intragranular character. The formation of a cladding layer associated with such reactions is thought to contribute to the retention of nanostructures during the consolidation step.

Developing nanocomposite structures in the granular state is advantageous for several reasons. The use of nanocomposite powders allows for conventional powder processing techniques to be employed to form ceramic bodies. The microstructure development even at the

granular scale is sensitive to the presence of fast diffusion pathways (e.g., grain boundaries, microcracks, or dislocations) that can lead to variability in morphological development. In this work, the use of highly crystalline and chemically homogeneous starting materials was found to significantly improve the consistency of microstructures in sintered ceramic nanocomposites, whose features are inherited from nanocomposite powder building blocks. The quality and consistency of feedstock materials for the proposed processing scheme is therefore critical to developing ceramic nanocomposites with tailored microstructures.

ACKNOWLEDGMENTS

This material is based upon work supported by, or in part by, the U. S. Army Research Laboratory and the U. S. Army Research Office under contract/grant number W911NF-14-1-0560. TEM and FIB work was supported by the University of Missouri Electron Microscopy Core "Excellence in Electron Microscopy" award. In addition, the authors thank Dr. Eric Bohannan (Missouri S&T) for assistance related to XRD materials characterization.

ORCID

David W. Lipke https://orcid.org/0000-0002-4557-6690

REFERENCES

1. Niihara K. New design concept of structural ceramics ceramic nanocomposites. J Ceram Soc Jpn. 1991;99(1154):974–82.
2. Zhao J, Stearns LC, Harmer MP, Chan HM, Miller GA, Cook RF. Mechanical behavior of alumina–silicon carbide "nanocomposites". J Am Ceram Soc. 1993;76(2):503–10.
3. Nawa M, Yamazaki K, Sekino T, Niihara K. A new type of nanocomposite in tetragonal zirconia polycrystal-molybdenum system. Mater Lett. 1994;20(5–6):299–304.
4. Sun X, Li JG, Guo S, Xiu Z, Duan K, Hu XZ. Intragranular particle residual stress strengthening of Al_2O_3–SiC nanocomposites. J Am Ceram Soc. 2005;88(6):1536–43.
5. Mukhopadhyay A, Todd RI. Microstructure and mechanical properties of Al_2O_3 matrix nanocomposites produced by solid state precipitation. J Eur Ceram Soc. 2010;30(6):1359–72.
6. Taya M, Hayashi S, Kobayashi AS, Yoon HS. Toughening of a particulate-reinforced ceramic–matrix composite by thermal residual stress. J Am Ceram Soc. 1990;73(5):1382–91.
7. Ferroni LP, Pezzotti G. Evidence for bulk residual stress strengthening in Al_2O_3/SiC nanocomposites. J Am Ceram Soc. 2002;85(8):2033–8.
8. Thompson AM, Chan HM, Harmer MP, Cook RE. Crack healing and stress relaxation in Al_2O_3–SiC "nanocomposites". J Am Ceram Soc. 1995;78(3):567–71.
9. Wu H, Roberts SG, Derby B. Residual stress and subsurface damage in machined alumina and alumina/silicon carbide nanocomposite ceramics. Acta Mater. 2001;49(3):507–17.
10. Pezzotti G, Nishida T, Sakai M. Physical limitations of the inherent toughness and strength in ceramic–ceramic and ceramic–metal nanocomposites. J Ceram Soc Jpn. 1995;103(1201):901–9.
11. Winn AJ, Todd RI. Microstructural requirements for alumina–SiC nanocomposites. Br Ceram Trans. 1999;98(5):219–24.
12. Mukhopadhyay A, Basu B. Consolidation–microstructure–property relationships in bulk nanoceramics and ceramic nanocomposites: a review. Int Mater Rev. 2007;52(5):257–88.
13. Palmero P. Structural ceramic nanocomposites: a review of properties and powders' synthesis methods. Nanomaterials. 2015;5(2):656–96.
14. Komarneni S. Nanocomposites. J Mater Chem. 1992;2(12):1219–30.
15. Sternitzke M. Structural ceramic nanocomposites. J Eur Ceram Soc. 1997;17(9):1061–82.
16. Xu Y, Zangvil A, Kerber A. SiC nanoparticle-reinforced Al_2O_3 matrix composites: role of intra- and intergranular particles. J Eur Ceram Soc. 1997;17(7):921–8.
17. Daniel BS, Murthy VS, Murty GS. Metal–ceramic composites via in-situ methods. J Mater Process Technol. 1997;68(2):132–55.
18. Derby B. Ceramic nanocomposites: mechanical properties. Curr Opin Solid State Mater Sci. 1998;3(5):490–5.
19. Bhaduri S, Bhaduri SB. Recent developments in ceramic nanocomposites. JOM. 1998;50(1):44–51.
20. Moya JS, Lopez-Esteban S, Pecharroman C. The challenge of ceramic/metal microcomposites and nanocomposites. Prog Mater Sci. 2007;52(7):1017–90.
21. Wu H. Understanding residual stresses and fracture toughness in ceramic nanocomposites. Residual stresses in composite materials. Woodhead Publishing; 2014. p. 256–92.
22. Harmer MP, Chan HM, Miller GA. Unique opportunities for microstructural engineering with duplex and laminar ceramic composites. J Am Ceram Soc. 1992;75(7):1715–28.
23. Padture NP, Bennison SJ, Chan HM. Flaw-tolerance and crack-resistance properties of alumina–aluminum titanate composites with tailored microstructures. J Am Ceram Soc. 1993;76(9):2312–20.
24. Padture NP, Runyan JL, Bennison SJ, Braun LM, Lawn BR. Model for toughness curves in two-phase ceramics: II. Microstructural variables. J Am Ceram Soc. 1993;76(9):2241–7.
25. Lutz EH. Predictability of the mechanical properties of inclusion-containing ceramics. J Am Ceram Soc. 1994;77(7):1901–8.
26. Monteverde F, Melandri C, Failla S, Grohsmeyer RJ, Hilmas GE, Fahrenholtz WG. Escape from the strength-to-toughness paradox: bulk ceramics through dual composite architectures. J Eur Ceram Soc. 2018;38(8):2961–70.
27. Zhao C, Gao S, Yang T, Scherer M, Schultheiß J, Meier D, et al. Precipitation hardening in ferroelectric ceramics. Adv Mater. 2021;33(36):2102421.
28. Zheng M, Hou Y, Zhu M, Yan H. Nanodomains in metal/ferroelectric 0–3 type composites: on the origin of the strong piezoelectric effect. Scr Mater. 2018;145:19–22.
29. Du H, Lin X, Zheng H, Qu B, Huang Y, Chu D. Colossal permittivity in percolative ceramic/metal dielectric composites. J Alloys Compd. 2016;663:848–61.
30. Kundu TK, Chakravorty D. Nanocomposite films of lead zirconate titanate and metallic nickel by sol-gel route. Appl Phys Lett. 1995;66(26):3576–8.
31. Zhao K, Zheng M, Yan X, Zhu M, Hou Y. Tailored ceramic–metal piezocomposite energy harvester with high current output by

controlling the electrical impedance. ACS Appl Electron Mater. 2022;4(7):3679–85.
32. Piciacchio A, Lee SH, Messing GL. Processing and microstructure development in alumina–silicon carbide intragranular particulate composites. J Am Ceram Soc. 1994;77(8):2157–64.
33. Hampshire S, Kennedy T. Silicon nitride–silicon carbide micro/nanocomposites: a review. Int J App Ceram Technol. 2022;19(2):1107–25.
34. Ustundag E, Subramanian R, Vaia R, Dieckmann R, Sass SL. In situ formation of metal–ceramic microstructures, including metal–ceramic composites, using reduction reactions. Acta Metall Mater. 1993;41(7):2153–61.
35. Rousset A. Alumina–metal (Fe, Cr, $Fe_{0.8}Cr_{0.2}$) nanocomposites. J Solid State Chem. 1994;111(1):164–71.
36. Handwerker CA, Foecke TJ, Wallace JS, Kattner UR, Jiggets RD. Formation of alumina–chromia–chromium composites by a partial reduction reaction. Mater Sci Eng A. 1995;195:89–100.
37. Laurent C, Peigney A, Quénard O, Rousset A. Synthesis and mechanical properties of nanometric metal particles–ceramic matrix nanocomposites. Ceramic–Ceramic Compos. IV. 1997;201–3.
38. Ji Y, Yeomans JA. Processing and mechanical properties of Al_2O_3–5 vol.% Cr nanocomposites. J Eur Ceram Soc. 2002;22(12):1927–36.
39. Avishai A, Kaplan WD. Intergranular films in metal–ceramic composites and the promotion of metal particle occlusion. Int J Mater Res. 2004;95(4):266–70.
40. Santanach JG, Estournes C, Weibel A, Peigney A, Chevallier G, Laurent C. Mechanical and tribological properties of Fe/Cr–$FeAl_2O_4$–Al_2O_3 nano/micro hybrid composites prepared by spark plasma sintering. Scr Mater. 2011;64(8):777.
41. Morrissey A, O'Brien JR, Reimanis IE. Tailored metal–ceramic nanocomposites prepared by redox cycling of polycrystalline Ni-doped yttria-stabilized zirconia. Scr Mater. 2016;112:109–13.
42. Rogers KA, Trumble KP. Effect of reduction temperature on internal reduction microstructures. Scr Mater. 1998;39(1):103–8.
43. Travitzky N, Fu Z, Knyazeva A, Janssen R, Nekludov D, Yin X, et al. Reactive synthesis of ceramic–metal composites. Adv Eng Mater. 2018;20:1800324.
44. Fahrenholtz WG. Reactive processing in ceramic-based systems. Int J Appl Ceram Tech. 2006;3(6):1–12.
45. Chiang Y-M, Haggerty JS, Messner RP, Demetry C. Reaction-based processing methods for ceramic–matrix composites. Ceram Bull. 1989;68(2):420–8.
46. Jia P, Chen L, Wang Y, Liu Z, Ouyang J, Zhang X, et al. Insights into intragranular precipitation and toughening effect of W in (Ti,W)C solid solution with TiH_2 as the inducer. Ceram Int. 2019;45:20626–33.
47. Chen S, Liu G, Yi F, Chen L, Liu Z, Fu Y, et al. The influence of Ti-induced precipitates on the microstructure and mechanical properties of (Zr,W)C solid solution. Mater Char. 2022;183:111604.
48. Garbiec D, Laptev AM, Leshchynsky V, Wisniewska M, Figiel P, Biedunkiewicz A, et al. Spark plasma sintering of WC–Ti powder mixtures and properties of obtained composites. J Eur Ceram Soc. 2022;42:2039–47.
49. Lipke DW, Zhang Y, Cai Y, Sandhage KH. Intragranular tungsten/zirconium carbide nanocomposites via a selective liquid/solid displacement reaction. J Am Ceram Soc. 2012;95(9):2769–72.
50. Miura A, Bartel CJ, Goto Y, Mizuguchi Y, Moriyoshi C, Kuroiwa Y, et al. Observing and modeling the sequential pairwise reactions that drive solid-state ceramic synthesis. Adv Mater. 2021;33(24):2100312.
51. Dempsey RD, Lipke DW. Gas–solid displacement reactions in the Ti–W–C system. J Am Ceram Soc. 2020;103(4):2376-88.
52. Narayan J, Chen Y. Physical properties of oxides containing metal precipitates. Phil Mag A. 1984;49(4):475–92.
53. Dempsey RD, Lipke DW. Effects of aluminum metal flux heat treatments on titanium–tungsten mixed carbide powders. J Solid State Chem. 2022;315:123541.
54. Bale CW, Belisle E, Chartrand P, Decterov S, Eriksson G, Gheribi AE, et al. FactSage thermochemical software and databases, 2010–2016. Calphad. 2016;54:35–53.
55. He X, Varley J, Ercius P, Erikson T, Bailey J, Zapalac G, et al. Intermixing and formation of Cu-rich secondary phases at sputtered CdS/$CuInGaSe_2$ heterojunctions. IEEE J Photovolt. 2016;6(5):1308–15.
56. Pennycook SJ, Jesson DE. High-resolution *Z*-contrast imaging of crystals. Ultramicroscopy. 1991;37(1–4):14–38.
57. Schindelin J, Arganda-Carreras I, Frise E, Kaynig V, Longair M, Pietzsch T, et al. Fiji: an open-source platform for biological-image analysis. Nat Methods. 2012;9(7):676–82.
58. Kracum MR, Marvel CJ, Albu M, Hofer F, Harmer MP, Chan HM. Copper–alumina nanocomposites derived from $CuAlO_2$: phase transformation and microstructural coarsening. J Am Ceram Soc. 2018;101(12):5801–10.
59. Backhaus-Ricoult M, Peyrot-Chabrol A. Diffusion-induced grain-boundary migration during internal reduction of chromium-doped Al_2O_3. Phil Mag A. 1996;73(4):973–98.
60. Holt JB, Munir ZA. Combustion synthesis of titanium carbide: theory and experiment. J Mater Sci. 1986;21(1):251–9.

SUPPORTING INFORMATION

Additional supporting information can be found online in the Supporting Information section at the end of this article.

How to cite this article: Dempsey RD, He X, Scott JA, Lipke DW. Intragranular nanocomposite powders as building blocks for ceramic nanocomposites. J Am Ceram Soc. 2023;1–10. https://doi.org/10.1111/jace.19175